Semimetallic and semiconducting graphene-*h*BN multilayers with parallel or reverse stacking

Xi Chen,[1,2] Klaus Zollner,[3] Christian Moulsdale,[1,2] Vladimir I. Fal'ko,[1,2,4] and Angelika Knothe [1,3]

[1]*National Graphene Institute, University of Manchester, Manchester M13 9PL, United Kingdom*
[2]*Department of Physics and Astronomy, University of Manchester, Oxford Road, Manchester M13 9PL, United Kingdom*
[3]*Institut für Theoretische Physik, Universität Regensburg, D-93040 Regensburg, Germany*
[4]*Henry Royce Institute for Advanced Materials, University of Manchester, Manchester M13 9PL, United Kingdom*

We theoretically investigate three-dimensional (3D) layered crystals of alternating graphene and *h*BN layers with different symmetries. Depending on the hopping parameters between the graphene layers, we find that these synthetic 3D materials can feature semimetallic, gapped, or Weyl semimetal phases. Using first-principles calculations to parametrize the low-energy Hamiltonians we establish the most likely electronic phases. Our results demonstrate that 3D crystals stacked from individual 2D materials represent a synthetic materials class with emergent properties different from their constituents.

I. INTRODUCTION

Thanks to the recent progress in the layer-to-layer assembly of two-dimensional atomic lattices, it is now possible to combine individual atomic layers to create advanced synthetic crystals that would be difficult to achieve with any other bottom-up technique. Such layered three-dimensional (3D) materials with engineered stacking series can exhibit emergent characteristics different from the properties of their individual constituent layers. Moreover, such assembly of layers allows for multiple stacking orders of consecutive layers with different symmetries. Therefore, 3D crystals obtained from stacking individual atomic layers one by one represent a synthetic materials class compared to the individual 2D sheets and their few-layer counterparts [1].

One widespread choice is to combine graphene with hexagonal boron nitride (*h*BN). Heterostructures of various numbers and stacking arrangements of graphene and *h*BN layers feature, e.g., diverse superlattice moiré effects [2–9], topological states [10,11], correlated states and superconductivity [12,13], dielectric and ferroelectric properties [14–16], and exotic Hofstadter butterflies [17,18].

Here, we provide both hybrid tight-binding-$k \cdot p$-theory and density functional theory (DFT) calculations for the low-energy states of 3D synthetic crystals constructed from alternately stacked graphene and *h*BN monolayers. At a single interface between graphene and *h*BN monolayers, the two lattices have slightly different lattice constants and straining one lattice to fit the lattice constant of the other is energetically very costly [19]. However, in a 3D bulk system with *h*BN layers alternating on either side of each monolayer graphene, the adhesion energy would promote the favorable atomic stacking of carbon and boron/nitrogen atoms. In compliance with recent first-principles [20] and diffusion Monte Carlo calculations [19] our DFT results confirm the interplay of adhesion and strain to favor carbon atoms to align with boron atoms to minimize the total energy [4,21].

We study periodic 3D stacking obtained by translating the *h*BN layers in the stacking process (hence all *h*BN layers are

parallel to each other; cf. Fig. 1). For this perfectly *z*-periodic Gr/*h*BN stack we study the resulting 3D band structures.

In a formal parametrization of the low-energy Hamiltonian, we find that, depending on the interlayer graphene hopping parameters, such a 3D crystal can feature different types of semimetallic spectra, including overlapping electron and hole pockets, as well as type I and type II Weyl cones. Such Weyl semimetals are 3D phases of matter whose electronic
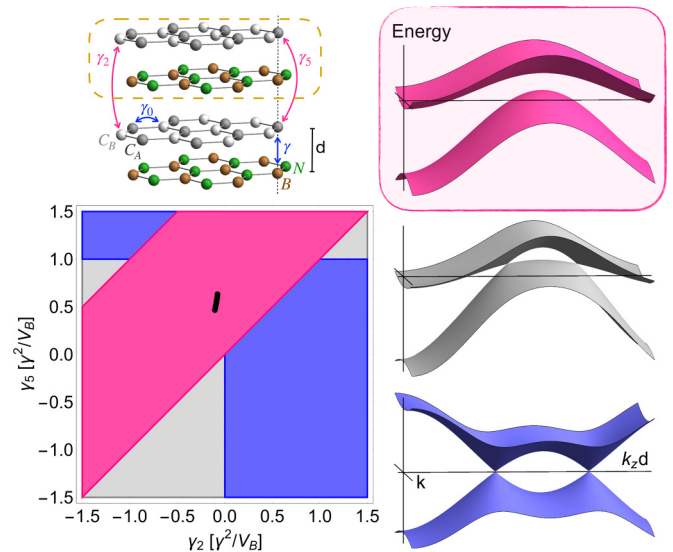

FIG. 1. Possible electronic phases for 3D crystals of graphene and *h*BN monolayers periodically stacked in the *z* direction (sketch on the top left, where the dashed orange line indicates the unit cell). Depending on the hopping parameters γ_5 and γ_2 between graphene sheets, this artificial material may exhibit different semimetal phases illustrated by the dispersion sketches. The black mark in the parameter map indicates parameter values we obtain from DFT calculations yielding the range $\gamma_5 \in \{0.48\,\gamma^2/V_B, 0.64\,\gamma^2/V_B\}$ and $\gamma_2 \in \{-0.10\,\gamma^2/V_B, -0.07\,\gamma^2/V_B\}$ with increasing interlayer distance d, identifying overlapping bands as the most likely phase (pink regime).

properties and topology entail protected surface states and anomalous responses to external electric and magnetic fields [22–28]. Subsequently, we use DFT calculations to obtain estimates for the coupling parameters and establish the actual phase of the 3D Gr/hBN crystal to feature overlapping, non-topological bands; cf. Fig. 1.

This manuscript is structured as follows. In Secs. II A and II B, we discuss the low-energy effective Hamiltonian for 3D Gr/hBN stacks with parallel hBN layers yielding the phase diagram of Fig. 1. In Sec. II C we present our DFT calculations used to parametrize the hopping parameters and to determine the most likely phase. In Sec. III we consider an alternative stacking sequence, where the hBNs are alternatingly rotated before placing them onto the graphene, resulting in adjacent hBN crystals in every second layer being antiparallel to each other (cf. Fig. 4). For this case of antiparallel stacking of hBN layers, we again analyze the resulting 3D band structures in terms of the low-energy Hamiltonian and complimentary DFT calculations. We discuss our results in Sec. IV and give details of the derivations and DFT calculations in the Appendixes.

II. PARALLEL STACKING

A. Phenomenological low-energy effective Hamiltonian

Starting from a hybrid $k \cdot p$ theory tight-binding approach [29] for the 3D graphene/hBN crystal we derive the low-energy effective Hamiltonian for the electrons on the graphene layers subject to perturbations from the adjacent hBNs [3,30,31]. Hybridization between graphene and hBN orbitals has been studied previously and used in earlier studies of, e.g., moiré superlattices of single Gr/hBN interfaces [8]. Here, we use second order perturbation theory in the interlayer hoppings to exclude the boron and nitrogen bands (see Appendix A for details of the calculation). For the 3D Gr/hBN stacks with translated (parallel, p) hBN layers as depicted in Fig. 1, the resulting low-energy Hamiltonian for the electrons in graphene reads

$$
H_{\rm p}
$$
$$
= \begin{pmatrix} -\frac{2\gamma^2}{V_B}[1+\cos(2k_z d)]+2\gamma_5\cos(2k_z d) & v\pi^\dagger \\ v\pi & 2\gamma_2\cos(2k_z d) \end{pmatrix},
$$
(1)

operating in the space spanned by the two-component wave function $\Psi = (\psi_{C_A}, \psi_{C_B})$ describing electronic amplitudes on the C_A and C_B sites of the graphene lattice. Further, $\pi = p_x + ip_y$ ($\mathbf{p} = -i\hbar\nabla$), V_B is the on-site potential of boron measured with respect to the on-site potentials of carbon, $v = \frac{\sqrt{3}a}{2}\gamma_0$ is the Fermi velocity, and d is the distance between graphene and hBN as indicated in Fig. 1.

For a faithful description of low-energy features in the electronic structure it is crucial to retain all the relevant couplings between different atomic sites [30]. Here, we take into account γ (between carbon and boron atoms), as well as the interlayer coupling parameters between graphene layers γ_5 and γ_2 between the in-equivalent carbon atoms C_A (separated by a boron atom) and C_B (separated by a hollow position). The precise values of these hoppings are *a priori* unknown. To explore the full parameter space, we first treat γ_5 and γ_2 as

free parameters in relation to γ in the following discussion of possible phases. Then, in Sec. II C, we use DFT to estimate these parameters and establish the actual phase.

B. Semimetal band structures

The relative magnitude and sign of the hopping parameters between different atomic lattice sites determines the electronic properties of the 3D Gr/hBN crystals in Fig. 1.

We find that a 3D Gr/hBN crystal with parallelly oriented hBN layers either features overlapping electron and hole pockets or type I or type II Weyl points depending on the hopping parameters γ_2 and γ_5. Figure 1 demonstrates this parametric dependence of the electronic properties, showing the phase diagram in the plane spanned by the interlayer hoppings and examples for the distinct possible 3D band structure types that we obtain from diagonalizing $H_{\rm p}$ in Eq. (1). In the gapless phases, linear Weyl nodes [22,24,32–35] form at momentum points $\mathbf{k}_0 = (0, 0, k_{z0})$ with

$$
k_{z0} = \pm \frac{1}{2d} \arccos\left[-\frac{\gamma^2}{\gamma^2 + V_B(\gamma_2 - \gamma_5)} \right].
$$
(2)

These touchings can be type I Weyl nodes (closed or point-like Fermi surfaces, blue phase in Fig. 1) or type II Weyl nodes (overlap between electron and hole bands leading to open Fermi surfaces, gray phase in Fig. 1) [22,27,35], and we find them to be Chern-nontrivial with Chern numbers $C = \pm 1$.

C. Modeling of graphene-hBN multilayers with density functional theory

To estimate values for the parameters in Eq. (1) we perform electronic structure calculations of the 3D Gr/hBN stack in Fig. 1 by DFT [36] with QUANTUM ESPRESSO [37]. Self-consistent calculations are carried out with a k-point sampling of $36 \times 36 \times 18$. We use an energy cutoff for charge density of 480 Ry and the kinetic energy cutoff for wave functions is 60 Ry for the scalar-relativistic pseudopotentials with the projector augmented wave method [38] with the Perdew-Burke-Ernzerhof exchange correlation functional [39]. Spin-orbit coupling is not included in the calculations. DFT-D2 van der Waals corrections are also included [40–42].

Our DFT calculations confirm that the atomic arrangement in Fig. 1 is indeed the lowest energy configuration, where B atoms serve as dimer atoms for C atoms in graphene. For this lowest-energy stacking, we fit the parameters of the model Hamiltonian. We present the extracted values of the parameters as a function of the interlayer distance in Fig. 2. The black mark in the parameter plot of Fig. 1 corresponds to these DFT parameter values in Fig. 2. The resulting DFT band structure for the lowest energy configuration yields an interlayer distance of $d = 3.15$ Å and confirms the top right continuum model bands in Fig. 1 (pink phase). Based on these results we claim the most likely phase of the parallelly stacked 3D Gr/hBN crystal to feature separated, overlapping bands. We show the corresponding shape of the $E_F = 0$ Fermi surface in Fig. 3.

Note that a small lattice mismatch of graphene and hBN does lead to moiré patterns [3,43,44]. Therefore, one cannot
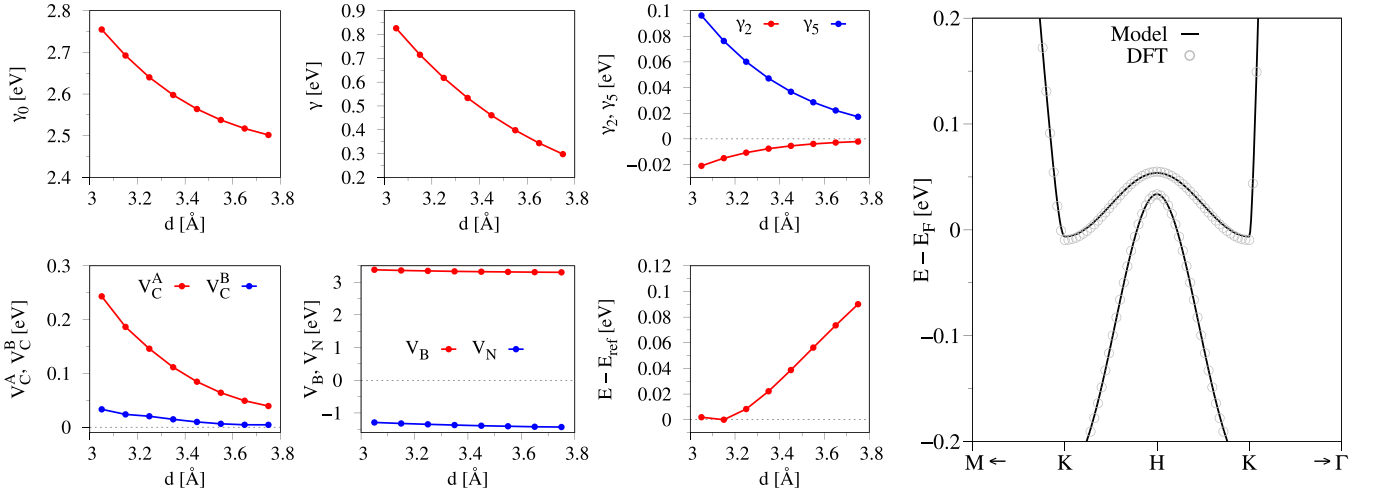
FIG. 2. Parameters obtained by fitting the model Hamiltonian [see Appendix B, Eq. (B1)] to the DFT-calculated low energy band structure, as a function of the layer spacing d. In the rightmost figure, we explicitly compare the DFT and model low energy band structure for the lowest energy distance $d = 3.15$ Å.

a priori exclude other stacking configurations within experimental setups. In Appendix B, we compare to the other commensurate high-symmetry stackings, where either N or both N and B atoms serve as dimer atoms. We also introduce model Hamiltonians, similar to above, and parametrize them according to the DFT results. We observe band touchings and conical band intersections for the parallel stacking configurations where graphene and nitrogen atoms dimerize; cf. Figs. 8 and 9 in Appendix B. Hence the electronic phase is determined by the stacking configuration. Reducing the interlayer distance, achievable with external pressure, does not lead to a phase transition. We explicitly demonstrate this in the Supplemental Material [45], where we show movies of the evolution of the band structures as a function of the interlayer

distance for the different stackings. However, since all commensurate high-symmetry stackings are potentially present in realistic experimental structures, the full phase diagram in Fig. 1 is physically relevant and one can expect local variations of the electronic phase in large scale samples.

III. ANTIPARALLEL STACKING

We turn to 3D Gr/hBN crystals where the adjacent hBN layers are rotated by 180° with respect to each other (antiparallel, ap; see the sketch in Fig. 4). In a similar fashion as for the parallel case we compute the low-energy Hamiltonian for antiparallel stacking,

$$H_{ap} = \begin{pmatrix} -\frac{2\gamma^2}{V_B} & v\pi^\dagger & e^{i4dk_z}\gamma_2 + \gamma_5 - \frac{\gamma^2}{V_B} & 0 \\ v\pi & -\frac{2\gamma^2}{V_B} & 0 & \gamma_2 + e^{i4dk_z}\left(\gamma_5 - \frac{\gamma^2}{V_B}\right) \\ e^{-i4dk_z}\gamma_2 + \gamma_5 - \frac{\gamma^2}{V_B} & 0 & -\frac{2\gamma^2}{V_B} & v\pi^\dagger \\ 0 & \gamma_2 + e^{-i4dk_z}\left(\gamma_5 - \frac{\gamma^2}{V_B}\right) & v\pi & -\frac{2\gamma^2}{V_B} \end{pmatrix}. \quad (3)$$

Note that the periodicity of the unit cell in the case of antiparallelly stacked hBN layers, Fig. 4, is twice as large compared to the case of parallel stacking; cf. Fig. 1. See Appendix A for details of the calculation.

We diagonalize H_{ap} in Eq. (3) to obtain the 3D band structures of Gr/hBN stacks with antiparallel arrangement of adjacent hBN layers. We compare different types of possible dispersions in Fig. 4 for different values of the couplings γ_5 and γ_2 (similar values as in the parallel case, Fig. 1, for the blue and magenta phase). We find gapless band structures for all coupling parameters as a consequence of the restored inversion symmetry of the antiparallel stacking configuration compared to the parallel one (the gray and the pink phase in Fig. 1 merge). The two electron bands and the two hole bands are degenerate, respectively, along k_z with $k_x = k_y = 0$. All

bands show conical band touchings at zero energy along a ring of radius

$$k_0' = \frac{1}{v}\left(\frac{\gamma^2}{V_B} - \gamma_2 - \gamma_5\right), \quad (4)$$

as well as for zero momentum at energies

$$\epsilon = \pm\frac{1}{V_B}\left(\sqrt{[\gamma^2 - (\gamma_2 + \gamma_5)V_B]^2} - \gamma^2\right) \quad (5)$$

in the conduction/valence band.

As in the case of parallelly stacked crystals, our DFT calculations confirm the lowest-energy stacking configuration and the results of the continuum model with the coupling
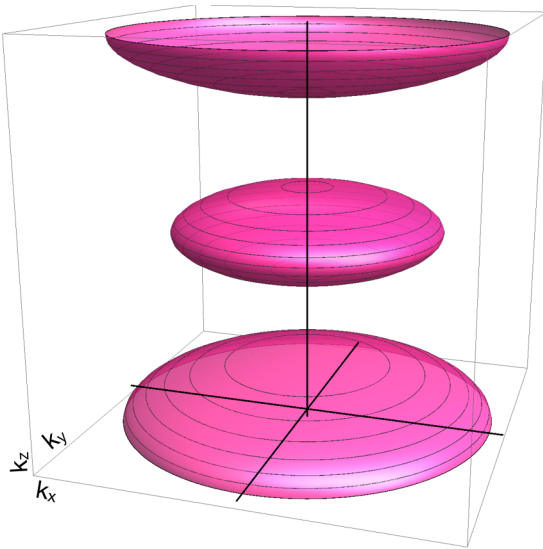
FIG. 3. Fermi surface for $E_F = 0$ of the overlapping bands of the parallelly stacked Gr/hBN 3D crystals that we identify using the parameters obtained from DFT.

FIG. 5. Conical crossings between the 3D bands of antiparallelly stacked Gr/hBN stacks at $k_z = 0$ that we determine for the parameters obtained from DFT. The white ring of radius k'_0 indicates the $E_F = 0$ Fermi line.

parameters of the magenta phase (rightmost panel in Fig. 4). We show the conical band touchings and the resulting $E_F = 0$ Fermi line for the set of parameters from DFT in Fig. 5.

IV. CONCLUSION

We presented the possible electronic structure of 3D stacks of alternating graphene and hBN layers with different symmetries. The atomic arrangements we consider represent the most stable configurations for carbon and boron/nitrogen atoms in single adjacent layers [19,20] as we confirm using DFT calculations. Since the hopping parameters between graphene atoms in different layers are *a priori* unknown, we identify regimes with different electronic properties (semimetallic, overlapping bands, and Weyl semimetals) upon varying these hoppings. We then extract estimates for the hopping parameters from DFT electronic structure calculations to determine
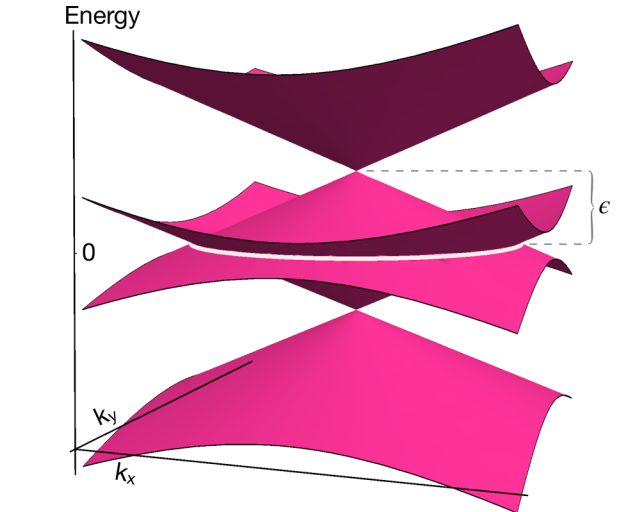
the most likely electronic phases. Regimes with different electronic band structures would make for distinctively different experimental signatures. Therefore, knowledge of the different possible types of dispersions presented here will help in identifying signatures of the band structure in both transport and spectroscopy experiments to confirm the relative sign and magnitude of these material parameters and set boundaries for their values. Moreover, we anticipate that these out-of-plane hopping parameters could be manipulated, e.g., by applying perpendicular pressure to the 3D stacks [46–48]. We hence confirm the stability of the electronic phase from DFT for different values of the interlayer distance.

Individual layers of graphene and hBN are very commonly combined in heterostructures with increasing precision and control, making the proposed crystals of alternating monolayers achievable in experiment. Using these 3D stacks of graphene and hBN as examples, we have demonstrated that artificial 3D crystals of individual atomic layers represent
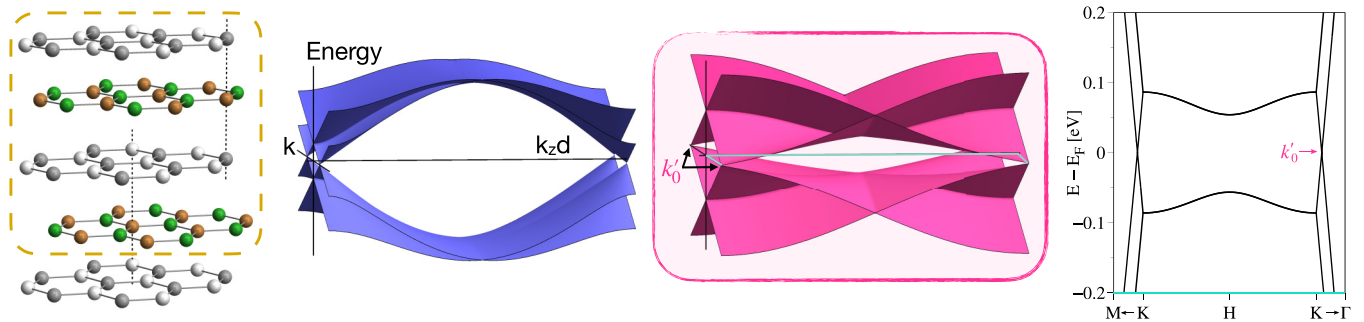

FIG. 4. Possible dispersions for 3D Gr/hBN crystals with antiparallel stacking, where adjacent hBNs in every second layer are rotated with respect to each other (sketch on the left). The dashed orange box illustrates that the unit cell in the z direction is twice as large for antiparallel stacking compared to parallel arrangements. We chose similar parameters as for the phases (blue, magenta) in Fig. 1. The phenomenological low-energy description in the magenta phase reproduces our DFT results (rightmost dispersion for a cut along the turquoise path in momentum space where the two electron bands and the two hole bands are degenerate, respectively).

an advanced synthetic 3D materials class with intriguing, potentially topologically nontrivial electronic properties only now achievable in experiments [1,49,50]. Besides the cases of alternating sequencing studied in this work, one may consider other stacking sequences with longer periods [51,52], stacking faults, interlayer twisting, and the combination of multiple different 2D materials. Such considerations are left for further studies.

APPENDIX A: DERIVATION OF THE LOW-ENERGY HAMILTONIANS

For the parallel stacking we start from the 4×4 Hamiltonian,

$$H = \begin{pmatrix} H_G & T^\dagger \\ T & H_{hBN} \end{pmatrix}, \tag{A1}$$

in the basis of the graphene and hBN atomic sites (C_A, C_B, N, B), where

$$H_G = \begin{pmatrix} V_C^A + 2\gamma_5 \cos(2k_z d) & v\pi^\dagger \\ v\pi & V_C^B + 2\gamma_2 \cos(2k_z d) \end{pmatrix},$$

$$H_{hBN} = \begin{pmatrix} V_N & 0 \\ 0 & V_B \end{pmatrix}, \quad T = (1 + e^{-i2k_z d})T_0,$$

$$T_0 = \frac{1}{3} \sum_{j=0}^{2} e^{i(\boldsymbol{K}_j - \boldsymbol{K}_0)\cdot\boldsymbol{r}_0} \begin{pmatrix} \gamma_N & \gamma_N e^{-i2\pi j/3} \\ \gamma_B e^{i2\pi j/3} & \gamma_B \end{pmatrix},$$

$$\boldsymbol{K}_j = \frac{4\pi}{3a}\left(\cos\frac{j2\pi}{3}, \sin\frac{j2\pi}{3}\right) \quad (j = 0, 1, 2), \tag{A2}$$

and for the relaxed equilibrium stacking considered in the main text the interlayer offset is $\boldsymbol{r}_0 = (0, \frac{a}{\sqrt{3}})$. Eliminating the hBN sites,

$$H_p = H_G + T^\dagger(-H_{hBN})^{-1}T, \tag{A3}$$

assuming $V_C^A, V_C^B \ll V_B$, and setting $\gamma \equiv \gamma_B$, we arrive at the expression in Eq. (1) of the main text.

Similarly, for the alternative antiparallel stacking, we start from the Hamiltonian,

$$\tilde{H} = \begin{pmatrix} H_{GG} & \tilde{T}^\dagger \\ \tilde{T} & H_{hBNhBN} \end{pmatrix}, \tag{A4}$$

in the basis of atoms on the upper and lower layers, $(C_A, C_B, \tilde{C}_A, \tilde{C}_B, N, B, \tilde{B}, \tilde{N})$, where

$$H_{GG} = \begin{pmatrix} V_C^A & v\pi^\dagger & \gamma_5 + e^{i4k_z d}\gamma_2 & 0 \\ v\pi & V_C^B & 0 & \gamma_2 + e^{i4k_z d}\gamma_5 \\ \gamma_5 + e^{-i4k_z d}\gamma_2 & 0 & V_C^A & v\pi^\dagger \\ 0 & \gamma_2 + e^{-i4k_z d}\gamma_5 & v\pi & V_C^B \end{pmatrix},$$

$$H_{hBNhBN} = \begin{pmatrix} V_N & 0 & 0 & 0 \\ 0 & V_B & 0 & 0 \\ 0 & 0 & V_B & 0 \\ 0 & 0 & 0 & V_N \end{pmatrix}, \quad \tilde{T} = \gamma \begin{pmatrix} 0 & 0 & 0 & 0 \\ 1 & 0 & 1 & 0 \\ 0 & e^{-i4k_z d} & 0 & 1 \\ 0 & 0 & 0 & 0 \end{pmatrix}. \tag{A5}$$

Then, we obtain H_{ap} in Eq. (3) via the usual transformation,

$$H_{ap} = H_{GG} + \tilde{T}^\dagger(-H_{hBNhBN})^{-1}\tilde{T}, \tag{A6}$$

for $V_C^A, V_C^B \ll V_B$.

APPENDIX B: DETAILS OF THE DFT CALCULATIONS

1. Structural information

Among the parallel configurations, we have three different choices to set up the unit cell [9]. The energetically most favorable is where C_A and B are dimer atoms, while C_B and N are nondimer atoms; see Fig. 6(a). The in-plane lattice constant is chosen to be $a = 2.4846$ Å, to compensate for the lattice mismatch between graphene and hBN [9]. Initial interlayer distances are summarized in the caption of Fig. 6. We also perform an interlayer distance study to find the energetically most favorable situation.
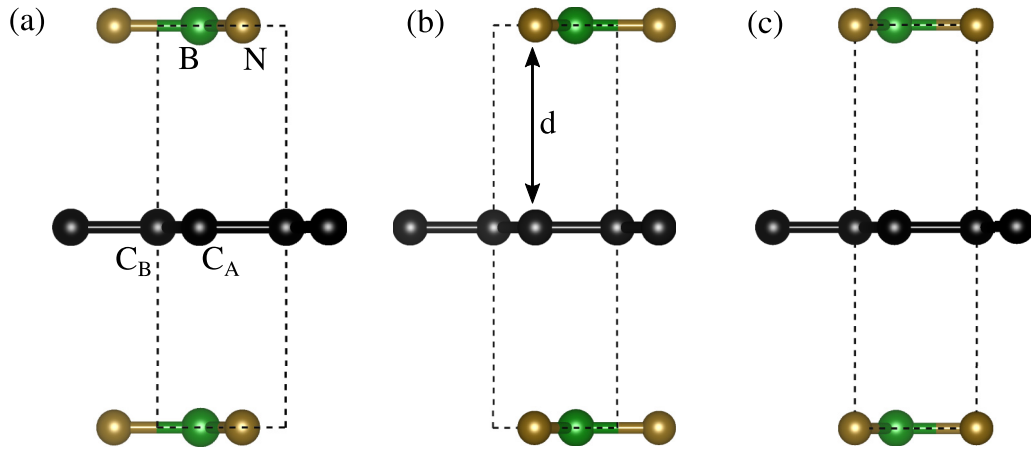
FIG. 6. Geometries of the parallel stacking configurations. The dashed lines represent the unit cell. (a) C_A and B are dimer atoms, while C_B and N are nondimer atoms. The interlayer distance $d = 3.35$ Å. (b) C_A and N are dimer atoms, while C_B and B are nondimer atoms. The interlayer distance $d = 3.50$ Å. (c) C_A and B, as well as C_B and N, are dimer atoms. The interlayer distance $d = 3.55$ Å. Initial interlayer distances from Ref. [9].
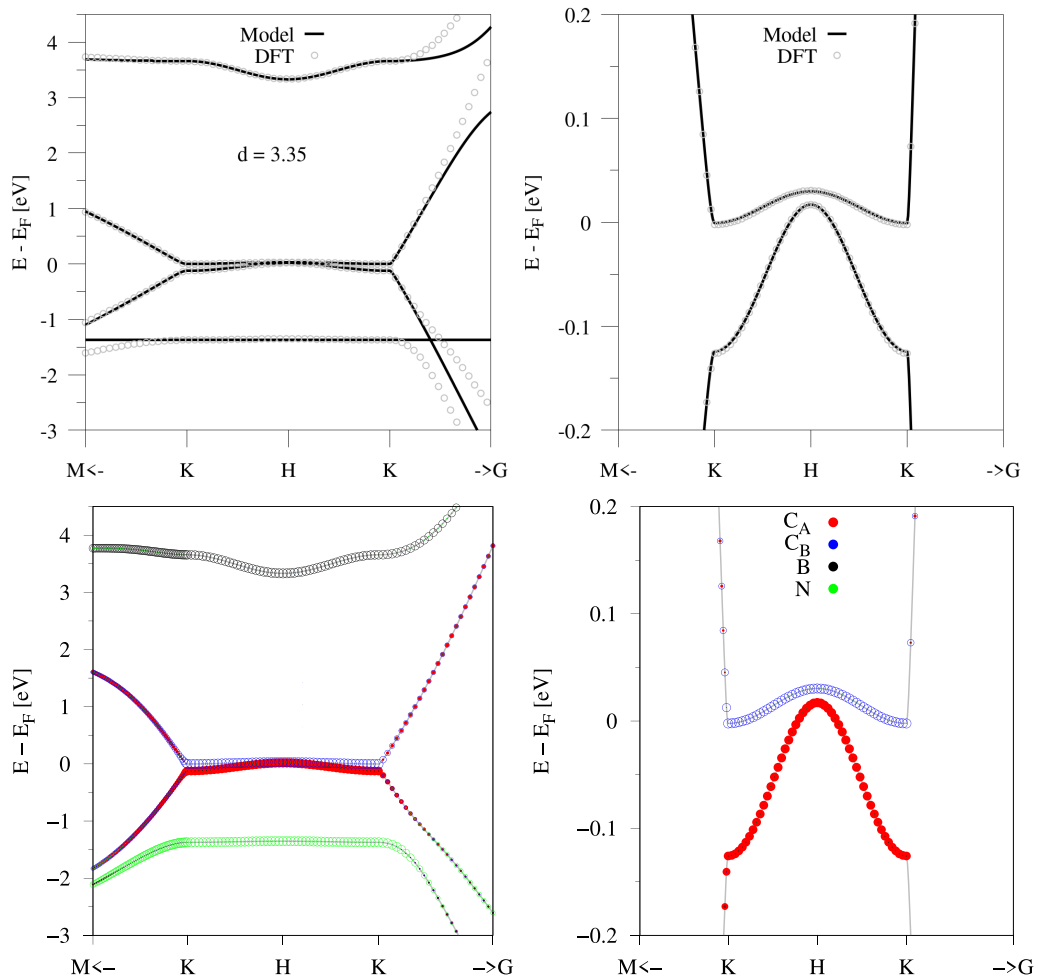

FIG. 7. Top: DFT and fit results for the geometry in Fig. 6(a). Bottom: the corresponding DFT-calculated projected band structure.

TABLE I. Fit parameters of the model Hamiltonian $\mathcal{H}_p^{(a)}$, for different interlayer distances. The reference energy is the lowest energy.

d (Å)	γ_0 (eV)	γ_1^B (eV)	γ_2 (eV)	γ_5 (eV)	V_C^A (eV)	V_C^B (eV)	V_B (eV)	V_N (eV)	$E - E_{\text{ref}}$ (eV)
3.05	2.75470	0.82614	−0.02102	0.09618	0.24316	0.03318	3.37880	−1.29091	0.00194
3.15	2.69242	0.71470	−0.01501	0.07636	0.18641	0.02375	3.35765	−1.32144	0
3.25	2.64012	0.61771	−0.01069	0.06018	0.14587	0.02035	3.34286	−1.34743	0.00833
3.35	2.59775	0.53364	−0.00761	0.04716	0.11139	0.01456	3.32984	−1.37067	0.02219
3.45	2.56400	0.46093	−0.00542	0.03679	0.08449	0.00978	3.31976	−1.39077	0.03876
3.55	2.53771	0.39811	−0.00388	0.02859	0.06399	0.00631	3.31176	−1.40743	0.05622
3.65	2.51729	0.34409	−0.00281	0.02219	0.04918	0.00449	3.30500	−1.42199	0.07354
3.75	2.50181	0.29784	−0.00205	0.01724	0.03928	0.00441	3.30070	−1.43176	0.09008

2. Model Hamiltonians to fit the DFT data

The model Hamiltonian for the geometry in Fig. 6(a) in the ordered basis (C_A, C_B, N, B) is

$$
\mathcal{H}_p^{(a)} = \begin{pmatrix}
V_C^A + 2\gamma_5 \cos(k_z c) & \gamma_0 f(\boldsymbol{k}) & 0 & \gamma_1^B[1 + \exp(ik_z c)] \\
\gamma_0 f^*(\boldsymbol{k}) & V_C^B + 2\gamma_2 \cos(k_z c) & 0 & 0 \\
0 & 0 & V_N & 0 \\
\gamma_1^B[1 + \exp(-ik_z c)] & 0 & 0 & V_B
\end{pmatrix},
\tag{B1}
$$

where V_C^A, V_C^B, V_B, and V_N are on-site potentials. The parameters γ_i, $i = \{0, 1, 2, 5\}$ correspond to intra- and interlayer hopping amplitudes [53], $f(\boldsymbol{k}) = e^{i\frac{a}{\sqrt{3}}k_y}[1 + 2 e^{-i\frac{\sqrt{3}a}{2}k_y} \cos(\frac{a}{2}k_x)]$ is the structural function of graphene, and $c = 2d$ is the lattice constant
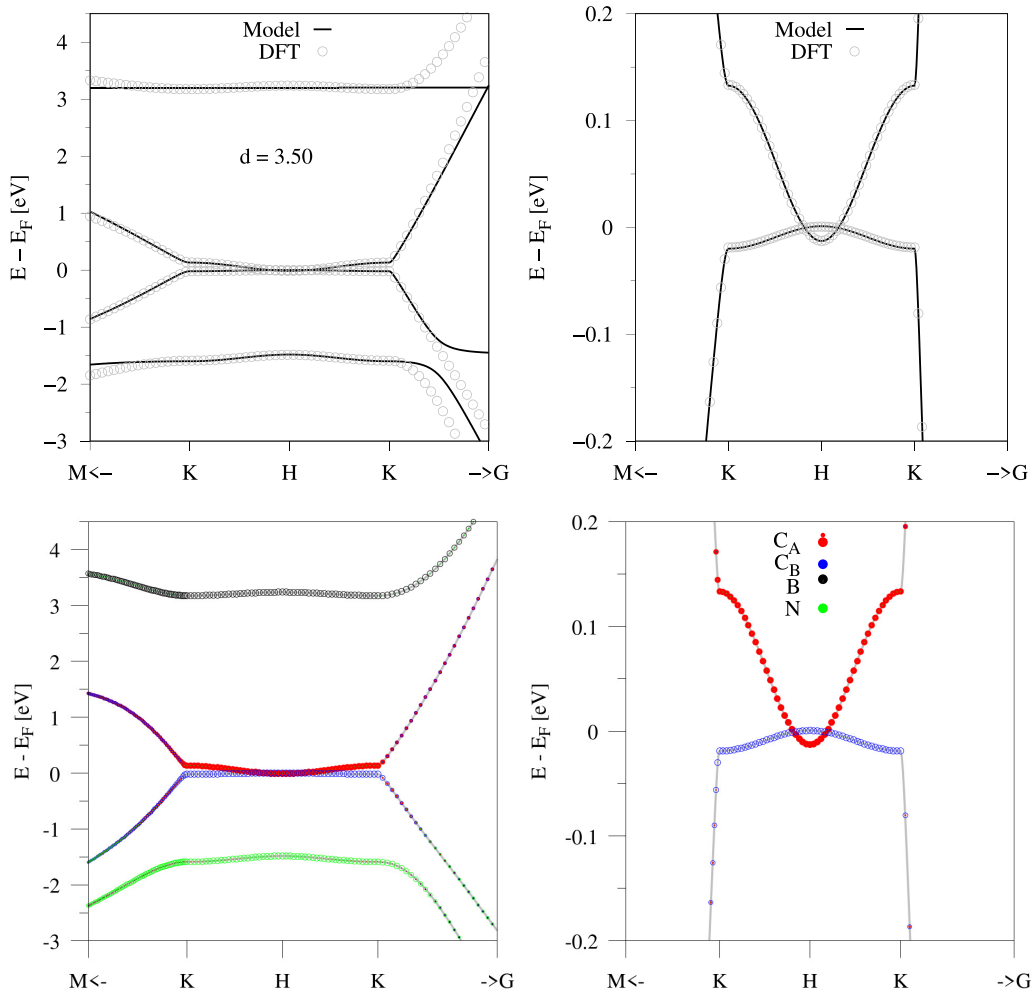

FIG. 8. Top: DFT and fit results for the geometry in Fig. 6(b). Bottom: the corresponding DFT-calculated projected band structure.
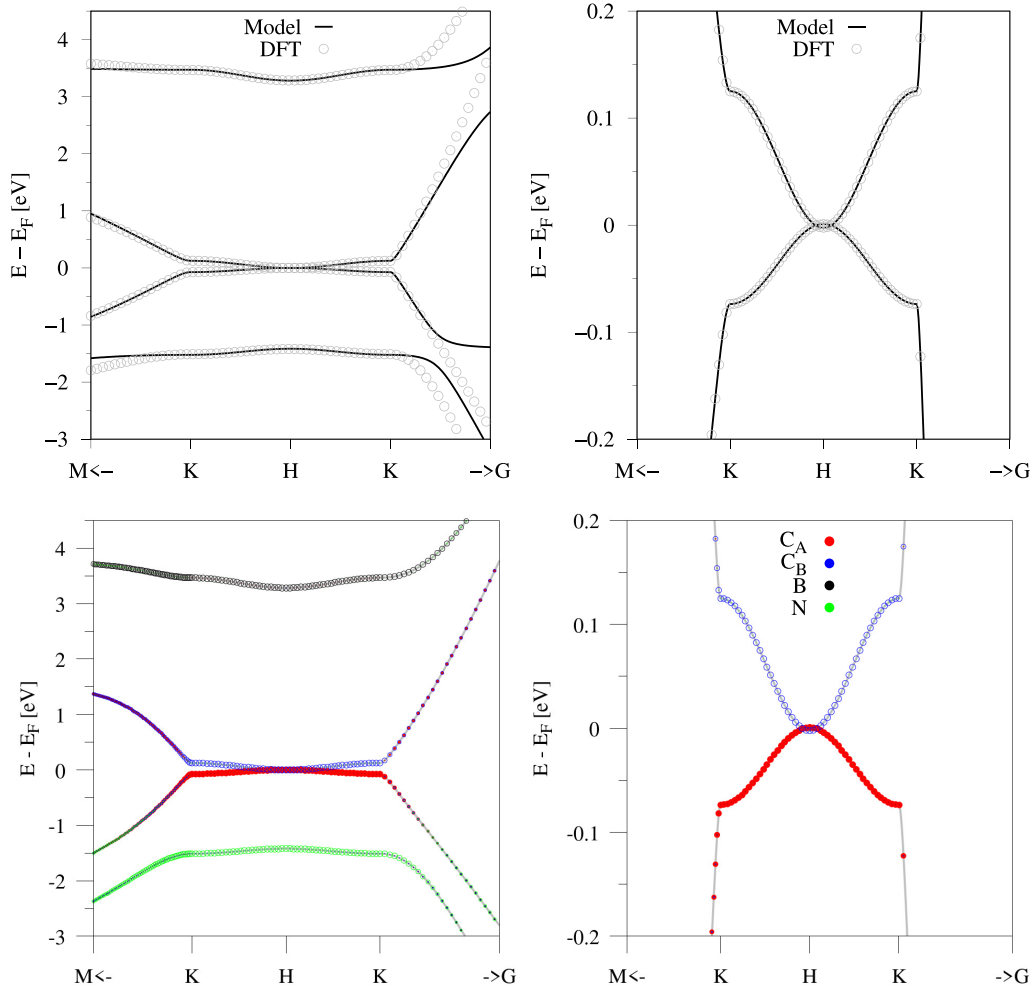
FIG. 9. Top: DFT and fit results for the geometry in Fig. 6(c). Bottom: the corresponding DFT-calculated projected band structure.

in z direction. In analogy, the model Hamiltonian for the geometry in Fig. 6(b) in the ordered basis (C_A, C_B, B, N) is

$$\mathcal{H}_p^{(b)} = \begin{pmatrix} V_C^A + 2\gamma_5 \cos(k_z c) & \gamma_0 f(\boldsymbol{k}) & 0 & \gamma_1^N [1 + \exp(ik_z c)] \\ \gamma_0 f^*(\boldsymbol{k}) & V_C^B + 2\gamma_2 \cos(k_z c) & 0 & 0 \\ 0 & 0 & V_B & 0 \\ \gamma_1^N [1 + \exp(-ik_z c)] & 0 & 0 & V_N \end{pmatrix}. \tag{B2}$$

TABLE II. Fit parameters of the model Hamiltonian $\mathcal{H}_p^{(b)}$, for different interlayer distances.

d (Å)	γ_0 (eV)	γ_1^N (eV)	γ_2 (eV)	γ_5 (eV)	V_C^A (eV)	V_C^B (eV)	V_B (eV)	V_N (eV)	$E - E_{\text{ref}}$ (eV)
3.10	2.25211	0.43522	−0.01971	0.02840	0.01380	−0.03399	3.01740	−1.55462	0.06995
3.20	2.29749	0.36510	−0.01411	0.02101	0.01076	−0.02424	3.08254	−1.52662	0.05677
3.30	2.33659	0.30670	−0.01012	0.01509	0.00725	−0.01751	3.13329	−1.50618	0.05485
3.40	2.36844	0.25815	−0.00728	0.01045	0.00388	−0.01285	3.17258	−1.49182	0.05987
3.50	2.39339	0.21790	−0.00525	0.00692	0.00113	−0.00941	3.20297	−1.48154	0.06919
3.60	2.41262	0.18494	−0.00380	0.00420	−0.00163	−0.00739	3.22568	−1.47470	0.08065
3.70	2.42711	0.15816	−0.00279	0.00213	−0.00355	−0.00568	3.24278	−1.47029	0.09328
3.80	2.43767	0.13657	−0.00207	0.00060	−0.00483	−0.00435	3.25588	−1.46734	0.10616

TABLE III. Fit parameters of the model Hamiltonian $\mathcal{H}_{p}^{(c)}$, for different interlayer distances.

d (Å)	γ_0 (eV)	γ_1^B (eV)	γ_1^N (eV)	γ_2 (eV)	γ_5 (eV)	V_C^A (eV)	V_C^B (eV)	V_B (eV)	V_N (eV)	$E - E_{\mathrm{ref}}$ (eV)
3.15	1.98206	0.71627	0.40386	0.02357	0.07780	0.16312	0.03231	3.25605	−1.36919	0.08568
3.25	2.13136	0.61940	0.33878	0.01722	0.06117	0.12664	0.02461	3.26689	−1.38102	0.07053
3.35	2.23663	0.53526	0.28458	0.01219	0.04781	0.09836	0.01829	3.27438	−1.39315	0.06710
3.45	2.30986	0.46237	0.23965	0.00829	0.03721	0.07588	0.01256	3.27816	−1.40536	0.07098
3.55	2.36046	0.39939	0.20266	0.00526	0.02885	0.05873	0.00795	3.28132	−1.41596	0.07920
3.65	2.39517	0.34524	0.17246	0.00295	0.02235	0.04590	0.00457	3.28350	−1.42555	0.08985
3.75	2.41887	0.29884	0.14800	0.00123	0.01732	0.03626	0.00219	3.28483	−1.43317	0.10162
3.85	0.25930	0.259298	0.12843	-5.06750×10^{-5}	0.01347	0.02865	5.07040×10^{-5}	3.28621	−1.43986	0.11372

Finally, the model Hamiltonian for the geometry in Fig. 6(c) in the ordered basis (C_A, C_B, N, B) is

$$
\mathcal{H}_{p}^{(c)} =
\begin{pmatrix}
V_C^A + 2\gamma_5 \cos(k_z c) & \gamma_0 f(\boldsymbol{k}) & 0 & \gamma_1^B[1 + \exp(ik_z c)] \\
\gamma_0 f^*(\boldsymbol{k}) & V_C^B + 2\gamma_2 \cos(k_z c) & \gamma_1^N[1 + \exp(ik_z c)] & 0 \\
0 & \gamma_1^N[1 + \exp(-ik_z c)] & V_N & 0 \\
\gamma_1^B[1 + \exp(-ik_z c)] & 0 & 0 & V_B
\end{pmatrix}.
\tag{B3}
$$

3. Results

In Fig. 7, we provide the DFT and fit results for the geometry in Fig. 6(a) for an interlayer distance of 3.35 Å. The minimal model Hamiltonian Eq. (B1) accurately reproduces the low energy bands, with the fit parameters summarized in Table I. We also provide a projected band structure to identify the sublattice contributions to the bands. In fact, the DFT results confirm that the energetically most favorable stacking results in a trivial (magenta) phase in the diagram of Fig. 1.

Similarly, we provide the DFT-calculated band structures with fit results for the other geometries in Figs. 8 and 9, with the model parameters summarized in Table II and Table III. We find that the other stacking configurations provide low energy bands in the nontrivial phase. So it is likely that, within a Gr/hBN moiré structure, both phases coexist.

Finally, the interlayer distance dependence of the model parameters, for all three stacking configurations, is summarized in Fig. 10. In the Supplemental Material [45] we also provide movies of the band structure evolution with the interlayer distance, demonstrating that a phase transition is not possible by tuning the distance.
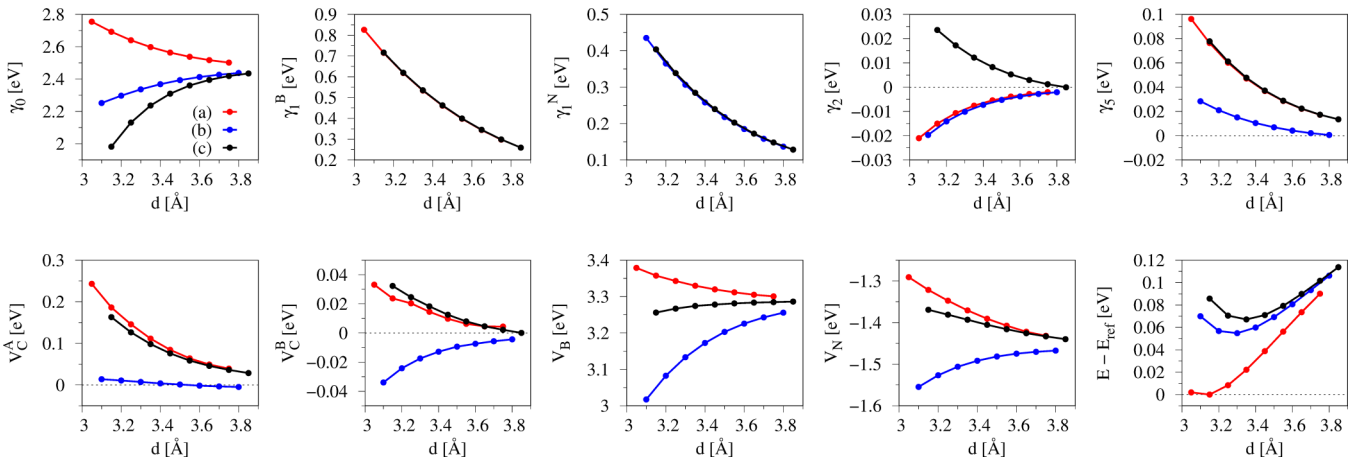

FIG. 10. Evolution of the fit parameters as a function of the interlayer distance, summarizing the results from Table I, Table II, and Table III.

[1] F. Liu, W. Wu, Y. Bai, S. H. Chae, Q. Li, J. Wang, J. Hone, and X.-Y. Zhu, Science **367**, 903 (2020).

[2] Z. Wang, Y. B. Wang, J. Yin, E. Tóvári, Y. Yang, L. Lin, M. Holwill, J. Birkbeck, D. J. Perello, S. Xu, J. Zultak, R. V. Gorbachev, A. V. Kretinin, T. Taniguchi, K. Watanabe, S. V. Morozov, M. Andelković, S. P. Milovanović, L. Covaci, F. M. Peeters, A. Mishchenko, A. K. Geim, K. S. Novoselov, V. I. Fal'ko, A. Knothe, and C. R. Woods, Sci. Adv. **5**, eaay8897 (2019).

[3] P. Moon and M. Koshino, Phys. Rev. B **90**, 155406 (2014).

[4] Y. Sakai, T. Koretsune, and S. Saito, Phys. Rev. B **83**, 205434 (2011).

[5] Y. Yang, J. Li, J. Yin, S. Xu, C. Mullan, T. Taniguchi, K. Watanabe, A. K. Geim, K. S. Novoselov, and A. Mishchenko, Sci. Adv. **6**, eabd3655 (2020).

[6] L. Wang, S. Zihlmann, M.-H. Liu, P. Makk, K. Watanabe, T. Taniguchi, A. Baumgartner, and C. Schönenberger, Nano Lett. **19**, 2371 (2019).

[7] N. R. Finney, M. Yankowitz, L. Muraleetharan, K. Watanabe, T. Taniguchi, C. R. Dean, and J. Hone, Nat. Nanotechnol. **14**, 1029 (2019).

[8] J. R. Wallbank, M. Mucha-Kruczyński, X. Chen, and V. I. Fal'ko, Ann. Phys. (Leipzig) **527**, 359 (2015).

[9] K. Zollner, M. Gmitra, and J. Fabian, Phys. Rev. B **99**, 125151 (2019).

[10] C. Hu, V. Michaud-Rioux, W. Yao, and H. Guo, Phys. Rev. Lett. **121**, 186403 (2018).

[11] C. Moulsdale, A. Knothe, and V. Fal'ko, Phys. Rev. B **105**, L201112 (2022).

[12] G. Chen, A. L. Sharpe, P. Gallagher, I. T. Rosen, E. J. Fox, L. Jiang, B. Lyu, H. Li, K. Watanabe, T. Taniguchi, J. Jung, Z. Shi, D. Goldhaber-Gordon, Y. Zhang, and F. Wang, Nature (London) **572**, 215 (2019).

[13] X. Sun, S. Zhang, Z. Liu, H. Zhu, J. Huang, K. Yuan, Z. Wang, K. Watanabe, T. Taniguchi, X. Li, M. Zhu, J. Mao, T. Yang, J. Kang, J. Liu, Y. Ye, Z. V. Han, and Z. Zhang, Nat. Commun. **12**, 7196 (2021).

[14] Q. Li, M. Liu, Y. Zhang, and Z. Liu, Small **12**, 32 (2016).

[15] Y. Wang, S. Jiang, J. Xiao, X. Cai, D. Zhang, P. Wang, G. Ma, Y. Han, J. Huang, K. Watanabe, T. Taniguchi, A. S. Mayorov, and G. Yu, Front. of Phys. **17**, 43504 (2022).

[16] Z. Zhu, S. Carr, Q. Ma, and E. Kaxiras, Phys. Rev. B **106**, 205134 (2022).

[17] X. Chen, J. R. Wallbank, M. Mucha-Kruczyński, E. McCann, and V. I. Fal'ko, Phys. Rev. B **94**, 045442 (2016).

[18] T. Fabian, M. Kausel, L. Linhart, J. Burgdörfer, and F. Libisch, Phys. Rev. B **106**, 165412 (2022).

[19] M. Szyniszewski, E. Mostaani, V. Enaldiev, A. C. Ferrari, and N. D. Drummond (private communication).

[20] G. Giovannetti, P. A. Khomyakov, G. Brocks, P. J. Kelly, and J. van den Brink, Phys. Rev. B **76**, 073103 (2007).

[21] I. V. Lebedeva, A. V. Lebedev, A. M. Popov, and A. A. Knizhnik, Comput. Mater. Sci. **128**, 45 (2017).

[22] N. P. Armitage, E. J. Mele, and A. Vishwanath, Rev. Mod. Phys. **90**, 015001 (2018).

[23] M. N. Chen, W. C. Chen, and Y. Zhou, J. Phys.: Condens. Matter **34**, 025502 (2022).

[24] A. A. Burkov, Annu. Rev. Condens. Matter Phys. **9**, 359 (2018).

[25] C. Zeng, S. Nandy, and S. Tewari, Phys. Rev. B **105**, 125131 (2022).

[26] S. Das, K. Das, and A. Agarwal, Phys. Rev. B **105**, 235408 (2022).

[27] T. M. Ballestad, A. Cortijo, M. A. H. Vozmediano, and A. Qaiumzadeh, Phys. Rev. B **107**, 014410 (2023).

[28] S. Das, K. Das, and A. Agarwal, arXiv:2301.02965.

[29] A. Garcia-Ruiz, H. Deng, V. V. Enaldiev, and V. I. Fal'ko, Phys. Rev. B **104**, 085402 (2021).

[30] E. McCann and V. I. Fal'ko, Phys. Rev. Lett. **96**, 086805 (2006).

[31] P. Giraud, Master's thesis, Université des Sciences et Technologies Lille 1 Universidad del Pais Vasco - Euskal Herriko Unibertsitatea, San Sebastian, Spain, 2012.

[32] J. Cayssol, C. R. Phys.Topolog. Insulat. / Isolants Topologiq.**14**, 760 (2013).

[33] C.-K. Chiu, J. C. Y. Teo, A. P. Schnyder, and S. Ryu, Rev. Mod. Phys. **88**, 035005 (2016).

[34] A. A. Burkov and L. Balents, Phys. Rev. Lett. **107**, 127205 (2011).

[35] M. O. Goerbig, J.-N. Fuchs, G. Montambaux, and F. Piéchon, Phys. Rev. B **78**, 045415 (2008).

[36] P. Hohenberg and W. Kohn, Phys. Rev. **136**, B864 (1964).

[37] P. Giannozzi *et al.*, J. Phys.: Condens. Matter **21**, 395502 (2009).

[38] G. Kresse and D. Joubert, Phys. Rev. B **59**, 1758 (1999).

[39] J. P. Perdew, K. Burke, and M. Ernzerhof, Phys. Rev. Lett. **77**, 3865 (1996).

[40] S. Grimme, J. Comput. Chem. **27**, 1787 (2006).

[41] S. Grimme, J. Antony, S. Ehrlich, and H. Krieg, J. Chem. Phys. **132**, 154104 (2010).

[42] V. Barone, M. Casarin, D. Forrer, M. Pavone, M. Sambi, and A. Vittadini, J. Comput. Chem. **30**, 934 (2009).

[43] J. Jung, A. Raoux, Z. Qiao, and A. H. MacDonald, Phys. Rev. B **89**, 205414 (2014).

[44] G. Argentero, A. Mittelberger, M. Reza Ahmadpour Monazam, Y. Cao, T. J. Pennycook, C. Mangler, C. Kramberger, J. Kotakoski, A. K. Geim, and J. C. Meyer, Nano Lett. **17**, 1409 (2017).

[45] See Supplemental Material at http://link.aps.org/supplemental/ 10.1103/PhysRevB.107.125402 where we provide movies of the band structure evolution with the interlayer distance as calculated from DFT for the different stacking configurations.

[46] B. Szentpéteri, P. Rickhaus, F. K. de Vries, A. Márffy, B. Fülöp, E. Tóvári, K. Watanabe, T. Taniguchi, A. Kormányos, S. Csonka, and P. Makk, Nano Lett. **21**, 8777 (2021).

[47] X. Lin, H. Zhu, and J. Ni, Phys. Rev. B **101**, 155405 (2020).

[48] M. Yankowitz, S. Chen, H. Polshyn, Y. Zhang, K. Watanabe, T. Taniguchi, D. Graf, A. F. Young, and C. R. Dean, Science **363**, 1059 (2019).

[49] F. Wu, R.-X. Zhang, and S. Das Sarma, Phys. Rev. Res. **2**, 022010(R) (2020).

[50] S. Wang, J. Crowther, H. Kageshima, H. Hibino, and Y. Taniyasu, ACS Nano **15**, 14384 (2021).

[51] A. García-Ruiz, S. Slizovskiy, M. Mucha-Kruczyński, and V. I. Fal'ko, Nano Lett. **19**, 6152 (2019).

[52] A. García-Ruiz, J. J. P. Thompson, M. Mucha-Kruczyński, and V. I. Fal'ko, Phys. Rev. Lett. **125**, 197401 (2020).

[53] Note that, in this part of the Appendix only, we explicitly write all the indices, i.e., $\gamma_1^B \equiv \gamma_B$.